Effect of oscillatory flow conditions on crystalliser fouling investigated through non-invasive imaging

Rachel Sheridan[a,b], Javier Cardona[a,b,c], Christos Tachtatzis[c], Yi-Chieh Chen[a], Alison Cleary[c], Naomi Briggs[d], Alastair Florence[b,d], Robert Atkinson[c], Craig Michie[c], Ivan Andonovic[c], Jan Sefcik[a,b,*]

[a] *Department of Chemical and Process Engineering, University of Strathclyde, Glasgow, G1 1XJ, Scotland, UK*
[b] *EPSRC Future Manufacturing Research Hub for Continuous Manufacturing and Advanced Crystallisation (CMAC), University of Strathclyde, Glasgow, G1 1RD, Scotland, UK*
[c] *Department of Electronic and Electrical Engineering, University of Strathclyde, Glasgow, G1 1XW, Scotland, UK*
[d] *Strathclyde Institute of Pharmaceutical and Biomedical Sciences, University of Strathclyde, Glasgow, G4 0RE, Scotland, UK*

Abstract

Conditions that lead to undesired fouling events in oscillatory flow crystallisers are investigated. The moving fluid oscillatory baffled crystalliser is used to mimic the operating conditions of continuous oscillatory baffled crystallisers, while reducing materials and energy consumption. A non-invasive imaging method is deployed to determine fouling induction times as a function of oscillatory flow conditions and supersaturation in crystallisation of glycine and L-glutamic acid from aqueous solutions. Heterogeneous nucleation kinetics are extracted from the distribution of fouling induction times, showing that higher fouling nucleation rates are observed when the frequency and amplitude of the oscillatory flow are increased. Higher oscillatory Reynolds numbers result in increased fluid shear in the crystalliser, promoting heterogeneous nucleation at the glass-solution interface and leading to subsequent fouling. It is therefore essential to consider the dependence of fouling kinetics on operating conditions to enable rational design of continuous crystallisers that ensure smooth and robust operation.

*Corresponding author
Email address: jan.sefcik@strath.ac.uk (Jan Sefcik)

This is a peer-reviewed, accepted author manuscript of the following article: Sheridan, R., Cardona, J., Tachtatzis, C., Chen, Y-C., Cleary, A., Briggs, N. E. B., Florence, A., Atkinson, R., Michie, C., Andonovic, I., & Sefcik, J. (2021). Effect of oscillatory flow conditions on crystalliser fouling investigated through non-invasive imaging. Chemical Engineering Science , [117188]. https://doi.org/10.1016/j.ces.2021.117188

Keywords: Fouling, Crystallisation, Oscillatory flow, MFOBC, Image Analysis

1. Introduction

In recent years, oscillatory flow reactors (OFRs) are attracting increasing attention as a means to enable transformation to continuous processing [1]. OFRs provide robust continuous operation under overall plug flow conditions while simultaneously enhancing mass and heat transfer through the oscillatory motion of the fluid on each of its sections [2, 3, 4, 5]. In particular, continuous oscillatory baffled crystallisers (COBC) create favourable conditions for crystallisation with reduced equipment dimensions in comparison with traditional plug flow reactors [6, 7, 8].

COBCs are usually formed by tubular jacketed straight sections with orifice baffles spaced equally throughout, as shown in Figure 1. Oscillation is generated through manipulating the frequency and amplitude of the flow via a motor, which powers a bellows mechanism. When coupled with the oscillatory flow, each cell of the COBC acts as an individual miniature stirred tank reactor with the ability to reach steady state. Efficient heat transfer and mixing are also achieved and close to plug flow conditions can be reached [9, 10, 11] when the operation is free of encrustation on the walls of the crystalliser. However, when the fluid oscillation conditions are not appropriately controlled, crystallisation enhancement can also promote encrustation or fouling of crystalline material on the walls of the reactor. This quickly becomes a major hurdle in continuous manufacturing environments as it can lead to shut down of the entire operation [6]. Therefore, understanding fouling mechanisms and kinetics in OFRs is key to their successful development for crystallisation processes.

Homogeneous nucleation where crystals spontaneously nucleate in the bulk solution is a rare occurrence. In most cases, heterogeneous nucleation dominates since this route has a more favourable energy pathway [12]. Excessive nucleation and growth on the walls of the crystalliser can lead to blockages, heat transfer reduction, unwanted crystal properties and false information from pro-

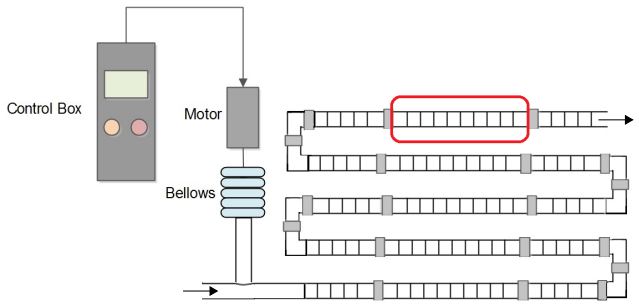

Figure 1: Diagram of a continuous oscillatory baffled crystalliser (COBC), with the region of interest for this study circled in red. The bottom left and top right arrows indicate the COBC inlet and outlet, respectively.

cess analytical technologies which are vital for process control [1, 13]. The time taken for fouling to reach a critical extent is of great interest since prevention or mitigation methods can be implemented, allowing a continuous crystallisation process to operate efficiently with appropriate measures in place. However, monitoring fouling is a challenging task.

Various direct and indirect approaches have been used to detect and monitor fouling in industrial sectors such as food processing [14, 15] and membrane separations [16]. Direct methods [16, 17, 18, 19, 20] rely on disassembling the fouled unit to measure the amount and chemical composition of the fouling material. Although these methods can be useful for understanding fouling phenomena, they are not suitable for on-line monitoring. In contrast, indirect methods enable non-invasive determination of fouling by studying its effect on process variables such as pressure drop [21], thermal resistance [21, 22, 23, 24], electrical resistance [25, 26], acoustic properties [27, 28] and moisture transfer in membrane processing [17, 29]. When a window into the process is available, in situ optical measurements become an appealing alternative [27].

In the crystallisation field, the focus of previous studies based on imaging is the characterisation of crystals in the bulk solution [30]. Crystal attributes have been extracted through both invasive probe-based techniques [31, 32, 33, 34, 35]

and non-invasive methods. The latter include the characterisation of crystal slurries [36] and the study of growth rates of specific crystal faces [37] via video microscopy with high-speed capture. Imaging techniques have also shown equivalent performance to other techniques such as focused beam reflectance measurement (FBRM) and UV/vis spectroscopy for determination of metastable zone widths [38]. Furthermore, more advanced approaches based on stereoscopic imaging have been implemented for the determination of 3D particle size in the bulk solution [39, 40, 41, 42, 43, 44]. In oscillatory baffled crystallisers, video imaging has been used to better understand the effect of its internal geometry on multiphase flow [45] and to determine crystal size distributions in the study of growth kinetics of paracetamol [46, 47]. The influence of the oscillatory flow conditions on crystal nucleation in the fluid bulk have also been investigated [48]. However, in all cases, crystals in the bulk solution were of interest and any crystal growth on surfaces was ignored. In this context, we recently showed in early trials that the use of video feeds for monitoring fouling is a promising method [49].

The aim of this paper is to study the conditions that lead to fouling in COBC setups via non-invasive imaging. In particular, we investigate how increasing the frequency and amplitude of the oscillatory flow effects fouling in crystallisation of glycine and L-glutamic acid from aqueous solutions. Two non-invasive methods are used to detect fouling and characterise it in terms of fouling induction times: 1) a visual inspection method and 2) an automated image processing algorithm. We then extract information on nucleation kinetics from the distribution of fouling induction times as a function of the operating conditions in the COBC.

2. Methods

2.1. Experimental setup

In order to understand the effect that the oscillatory flow conditions have on the fouling outcome, it would be useful to analyse a particular section of the COBC shown in Figure 1, without having to operate the equipment as a whole,

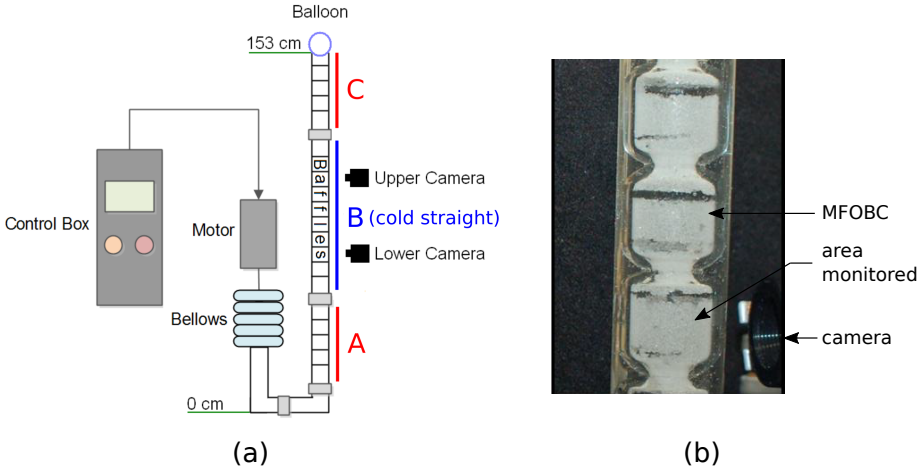

Figure 2: Moving Fluid Oscillatory Baffled Crystalliser (MFOBC). (a) Diagram of the experimental setup used in this work. The position of the cameras and the PTFE collars that connect the glass components together are indicated in the figure. The setup is divided in three different jacketed areas: the input straight (A), the crystallisation straight where the fluid is monitored (B), and the output straight open to the atmosphere (C). (b) Image of the MFOBC setup showing the position of one of the cameras.

reducing the consumption of raw materials and energy. With these considerations in mind, the moving fluid oscillatory baffled crystalliser (MFOBC), first introduced by Briggs [50], was the experimental platform selected for this study. It consists of DN15 glass components which are normally used to construct the larger COBC. The circled area in Figure 1 shows the glass straight of interest for monitoring fouling. This area was removed from the continuous setup and mounted vertically to create a batch system.

The final MFOBC experimental arrangement is shown in Figure 2(a). More details on this setup can be found in previous publications [49, 50]. Area B is the region of interest where cooling crystallisation occurs and fouling is expected. Two cameras are installed at the lower and upper end of this area to monitor the occurrence of fouling; an illustration of the position of one of the cameras is displayed in Figure 2(b). The boundary regions A and C are kept hot to prevent seeding and nucleation in the bellows and the balloon, respectively.

The balloon was placed over the top of the MFOBC – which is open to the air – to limit the effects of evaporation and avoid evaporative crystallisation. The temperatures of the different regions were calibrated using pure water to ensure that the crystallisation straight was always at the predefined temperature.

2.2. Experimental conditions

Hot supersaturated solution was pumped in to the MFOBC using a peristaltic pump via a port at the base of the equipment. The MFOBC was filled so that the upper half straight was approximately 75% full. At this point, the oscillation was initiated and temperatures were recorded as the experiment was run. The total volume of solution present in the equipment, including the fluid inside the unjacketed bellows section was approximately 420 ml in each experiment.

Glycine (purity $\geq$ 99%; CAS number 56-40-6) and β-L-glutamic acid (purity $\geq$ 98.5%; $\leq$ 0.1% of α form; CAS number 56-86-0), both purchased from Sigma-Aldrich, were chosen for analysis in the MFOBC due to the detailed data available on their solubility in water (glycine [51, 52]; L-glutamic acid [52, 53]). All the solutions were prepared using deionised water sourced from a Thermo Scientific Barnstead Reverse Osmosis water purification unit. Table 1 summarises the range of experimental conditions studied in this work. The concentrations of the aqueous solutions were chosen based on their corresponding values of supersaturation (S) at the crystallisation temperature in the cold straight.

In order to study the effect of the oscillation conditions on the occurrence of fouling, two different oscillation frequencies (i.e. 1 and 2 Hz) were applied to all experiments. For the experiments with L-glutamic acid, the amplitude of the flow oscillation was set to 45 mm—the equivalent to the height of two cells in the MFOBC. For glycine, two different oscillation amplitudes (i.e. 23 and 45 mm) were tested. In order to avoid crystallisation in the upper straight, the solution had to be kept hot enough. For L-glutamic acid, this could only be achieved at amplitude of 45 mm, where the heat transfer from the jacket was fast enough, as higher temperature was required than for glycine to prevent crystallisation on the upper straight. Greater amplitudes were unable to be achieved due to

System	Glycine				L-glutamic acid					
Temperature (°C)	20				20				30	
Concentration (g/L)	385				28.3		42.4			
Supersaturation [51, 52, 53]	1.8				4.0		6.0		4.2	
Amplitude (mm)	23		45		45					
Frequency (Hz)	1	2	1	2	1	2	1	2	1	2

Table 1: Summary of experimental conditions in the MFOBC.

the competing temperatures between the three glass straights in the system. Increasing the amplitude further meant that the chiller unit would have to run at lower temperatures. However, this resulted in condensation on the outer glass wall of the MFOBC making imaging of the region of interest impossible.

To ensure the reproducibility of the results, at least five repetitions were performed for each concentration and oscillation condition. All data underpinning this publication are openly available from the University of Strathclyde KnowledgeBase at https://doi.org/10.15129/6d07001a-ad6c-4e0b-bdbb-f8ebf74c142e.

2.3. Fouling detection methods

The objective of the non-invasive imaging technique described in this paper is to elicit more quantitative information on the effects the operating parameters of the MFOBC exert on fouling behaviour. During an experiment in the MFOBC, images were taken of the crystallisation straight at two independent positions (i.e. at two different heights; 66.5 cm and 88.0 cm), as shown in Figure 2(a). No preferential areas for fouling were observed under the conditions of this study. However, it is important to note that, for systems where fouling does not occur evenly in the crystalliser, more careful consideration of the position of the cameras may be required. Microsoft LifeCam VX-3000 webcams with manual adjustable focus were aligned with the center of MFOBC cells, as shown in Figure 2(b). The focus was sharpened so that the glass wall was clearly viewed. The YAWCAM software [54] was used to save simultaneous images from the two cameras every three seconds. The cameras were contained within

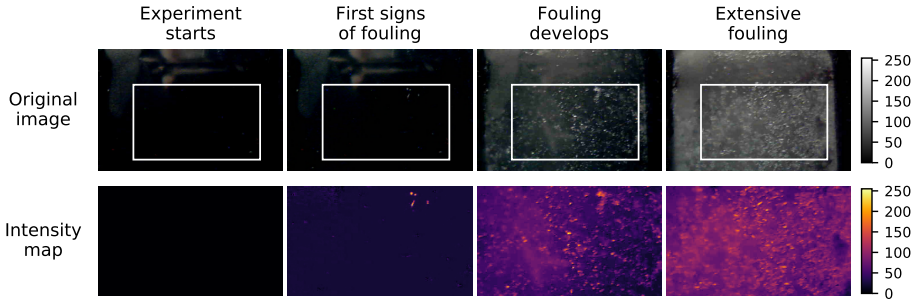

Figure 3: Visual inspection method for fouling detection. The white rectangle indicates the region analysed in the original image. In the resulting pixel intensity maps, bright areas correspond to denser fouling.

a box lined with black foam which was mounted to the MFOBC. An LED torch with a white diffuser was placed inside the box. This environment created suitable illumination conditions, making the experiments more reproducible and producing images of better quality.

The image sets generated in the experiments were further analysed. First, the images were converted to greyscale where all pixels were given a value between 0 (black) and 255 (white) based on their intensity. A threshold pixel intensity of 5 was set to eliminate noise in the images but still be sensitive enough to detect the first signs of fouling. The first image in the set, for which no fouling had yet occurred, was subtracted from every other image in the sequence to eliminate background effects. Then, as shown in Figure 3, a region of the image was defined to carry out the analysis. This region was the same for all image sets. Finally, two different methods were used for determination of fouling induction times:

(a) *Visual inspection method:* A pixel intensity heat map was generated to enable easier detection of fouling in the selected region – see Figure 3. Fouling induction times were obtained through visually inspecting the software interface as it ran through the image sequence. When growth on the wall commenced, the fouled pixels became more intense and persistent.

In contrast, crystallisation in the bulk had lower intensity since the camera was focused on the wall. Additionally, due to the oscillation of the flow, the distinction between material which was stationary (i.e. fouling) and material which was in constant motion (i.e. crystals in the bulk fluid) was clear. The fouling induction time was defined as the time when the first crystal appeared and persisted on the glass surface.

(b) *Automated image processing method:* An alternative method was developed to minimise human intervention in the determination of fouling induction times. The average pixel intensity of the selected region was plotted over time, as shown in Figure 4. The characteristic shape of the resulting curves with a noticeable intensity rise when fouling became more extensive gave the opportunity to automate the analysis. The fouling induction time is defined as the time at which the average pixel intensity of the region rises above a value of 10 and this condition persists for at least 10 consecutive frames. The latter condition is included to discard outliers. For example, Figure 4 shows an initial short pixel intensity spike that is due to an erroneous frame captured by the camera, as shown in Figure B.10 in the Appendix. Outliers could also be caused by the presence of bubbles or nucleation events in the bulk liquid. These occurrences are not to be confused with the persistent fouling event observed later. The specific persistence threshold of 10 frames is selected based on a sensitivity analysis of its effect on the mean fouling induction time for glycine and L-glutamic acid, as shown in Figure B.11 in the Appendix.

2.4. Analysis of fouling induction times

Fouling nucleation phenomena are usually characterised in terms of mean induction times. However, the experimentally measurable induction times are a convolution of two effects: the actual nucleation of a crystal on the wall of the crystalliser and the growth of this crystal until detectable sizes. Therefore, the

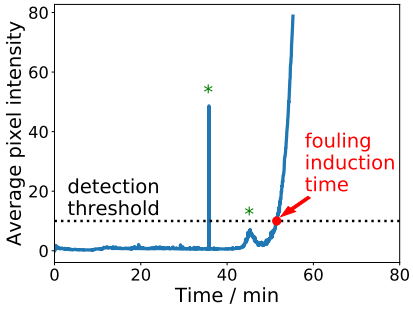

Figure 4: Automated image processing method for fouling detection. Evolution of the average pixel intensity of the analysed region with time. The red dot indicates the fouling induction time that corresponds to the indicated detection threshold (black dotted line). Green asterisks represent outliers.

190 determination of fouling induction times enables further study of both fouling nucleation rates and growth kinetics.

The experimental probability distribution of induction times is given by:

$$P(t) = \frac{M^+(t)}{M} \tag{1}$$

where $M^+(t)$ is the number of experiments where fouling is detected at time t and M is the total number of experiments.

Assuming time-independent nucleation rate, the probability distribution of induction times $P(t)$ can be described using a Poisson distribution [55]. The probability that at least one nucleus is created during a time interval $t - t_g$ is given by:

$$P(t) = 1 - \exp\left[-J\left(t - t_g\right)\right] \tag{2}$$

where J is the overall nucleation rate in terms of the number of nuclei formed per unit time in the region under observation, and t_g is the growth time, i.e. the time delay between the appearance of one crystal nucleus and the time required for this nucleus to grow to detectable sizes, t. Rearranging Equation 2 results in:

$$\ln\left[1 - P(t)\right] = -Jt + Jt_g \tag{3}$$

A linear fit of this model to the experimental cumulative probability distribution of induction times $P(t)$ using the least squares method leads to the determination of the nucleation rate J and the growth time t_g.

3. Results and discussion

Experiments were carried out in the MFOBC to establish the effect of oscillatory flow parameters (i.e. frequency and amplitude) on fouling induction times. The procedure to establish the desired temperature and supersaturation profiles in the MFOBC is presented first. This is followed by the determination of fouling induction times and corresponding nucleation kinetics for aqueous solutions of glycine and L-glutamic acid at different concentrations and oscillatory flow conditions.

3.1. Determination of temperature profiles in the MFOBC

The MFOBC was characterised to establish the temperature profiles within the equipment. This was achieved through adjusting the jacket temperatures of each glass straight (i.e. sections A, B and C in Figure 2(a)) in a calibration experiment with water. The following temperatures were crucial: 1) T_A, which should be high enough to avoid nucleation in the bellows section, 2) T_B, the crystallisation temperature in the cold straight, and 3) T_C, high enough so that nucleation was guaranteed to take place in the crystallisation straight first. By way of example, Figure 5 shows the temperature profile achieved in the calibration experiment when the target for T_B was set to 20°C. To rationalise the choices of temperature, the supersaturations along the height of the MFOBC were also calculated based on this measured temperature profile, using solubility data available in the literature for glycine [51, 52] and L-glutamic acid [52, 53]. Figure 5 includes the corresponding supersaturation profiles for aqueous solutions of L-glutamic acid at 21.2, 28.3 and 42.4 g/L. Examples of the actual temperature profiles recorded during the experiments with glycine and L-glutamic acid are shown in the Appendix (see Figure A.9(a) and Figure A.9(b), respectively).

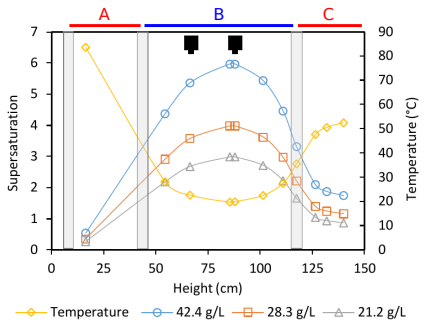

Figure 5: Temperature profile (yellow diamonds) obtained during calibration with pure water and expected supersaturation profiles for L-glutamic acid aqueous solutions at 42.4 g/L (blue circles), 28.3 g/L (orange squares) and 21.2 g/L (grey triangles). The position of the cameras and the PTFE collars (vertical bars) in the MFOBC are indicated in the figure, along with the extension of the input straight (A), the crystallisation straight (B), and the output straight (C).

Two crystallisation temperatures (T_B) were tested in the case of L-glutamic acid (i.e. 20°C and 30°C), while all experiments with glycine were performed at 20°C. After 3.5 hours of experiment, crystallisation was not achieved for glycine solutions at 299.06 g/L (S=1.4 at 20°C). The same situation was observed for the 21.2 g/L L-glutamic acid solution (S=3 at 20°C). Therefore, nucleation was hindered in the lower (A) and upper (C) straights of the MFOBC by keeping the temperature in these sections above a value that guaranteed supersaturations lower than 1.4 and 3 for glycine and L-glutamic acid, respectively. Heating of the upper straight also ensured that any undesired crystallisation at the top of the upper straight would be avoided as the walls would be periodically washed by a hot solution.

3.2. Fouling induction times

The temperature profiles defined in the previous section were applied to the set of experiments introduced in Table 1. The aim was to study the influence of oscillation conditions and solution supersaturation on fouling induction times in the MFOBC. The data obtained from the image-based fouling monitoring setup

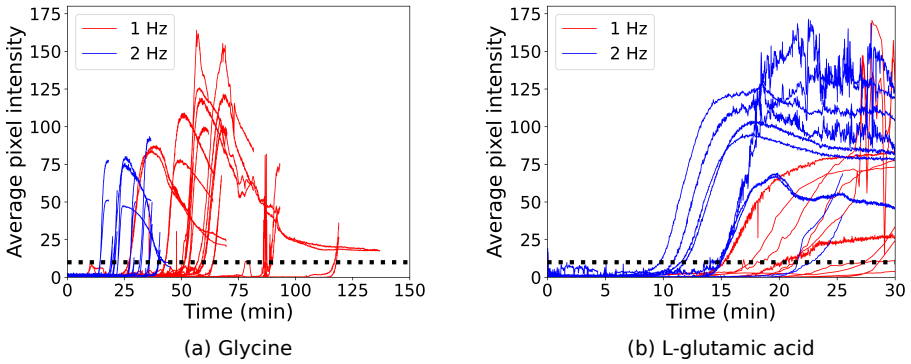

Figure 6: Evolution of average pixel intensity for (a) all glycine experiments at 20°C and 385 g/L (S=1.8) with an oscillation amplitude of 23 mm, and (b) all L-glutamic acid experiments at 20°C and 42.4 g/L (S=6) with an oscillation amplitude of 45 mm. The black dotted line represents the fouling detection threshold for the automated method.

were analysed to extract this information.

The time evolution of the average pixel intensity of the regions of interest, for several repetitions of glycine and L-glutamic acid fouling experiments at 20°C, are shown in Figure 6(a) and Figure 6(b), respectively. The experiments are performed under two different oscillatory flow frequencies (i.e. 1 Hz and 2 Hz). These figures include results from both the lower and the upper cameras since no significant differences were observed between the two regions under study. The curves have a characteristic sigmoidal shape where a sharp increase in average pixel intensity is triggered by the occurrence of fouling on the walls of the MFOBC. Despite the randomness of the nucleation events leading to fouling, a shift to shorter induction times is observed when the oscillation frequency is raised from 1 to 2 Hz for both systems. In some cases, an intensity drop is observed towards the end of the runs, likely due to detachment of encrustation after a certain level of deposition is achieved. An example of this behaviour is shown in Figure B.12 in the Appendix, where it is suspected that eddy formation around the baffles constriction generates higher local shear, which provide sufficient force to dislodge adhering solids.

In order to enable a simpler comparison between experimental conditions, the fouling events were quantified in terms of fouling induction times using both the visual inspection and the automated image processing methods previously described. The black dotted lines in Figure 6 illustrate the fouling detection threshold used by the automated method.

System	Operating conditions				Mean induction time (min)	
	T (°C)	S	f (Hz)	x_0 (mm)	Visual	Automated
Glycine	20	1.8	1	23	57 ± 6	61 ± 6
	20	1.8	2	23	24 ± 2	26 ± 2
	20	1.8	1	45	26 ± 3	28 ± 3
	20	1.8	2	45	11 ± 1	12 ± 1
L-glutamic acid	20	6	1	45	14 ± 2	22 ± 2
	20	6	2	45	9 ± 1	15 ± 2
	20	4	1	45	130 ± 30	170 ± 20
	20	4	2	45	80 ± 20	70 ± 8
	30	4.2	1	45	25 ± 4	36 ± 3
	30	4.2	2	45	11 ± 2	19 ± 2

Table 2: Mean induction times for glycine and L-glutamic acid experiments obtained with the visual inspection and the automated image analysis methods. The error values correspond to one standard deviation.

The resulting mean induction times for each set of conditions used in the glycine and L-glutamic acid experiments can be found in Table 2. Figure B.13 in the Appendix displays the individual fouling induction times used to calculate this mean. In general, good agreement is achieved between the fouling induction times provided by image processing and visual inspection methods, although the former tend to be slightly longer. This is expected since the visual inspection method can detect individual fouling events occurring early in the process while the automated image processing method provides an aggregated view through the average pixel intensity of the entire region of interest. More extended fouling coverage is required to trigger a detection in this case. Nevertheless, initial fouling by a limited number of single crystals on the glass walls is not a major

manufacturing concern. The fouling levels achieved when the image processing method generates a warning remain low and effective corrective actions can still be put in place.

On closer inspection, the fouling induction times for the glycine dataset reveal some key features of the effect of the oscillation conditions in the MFOBC. As observed in Table 2 and Figure B.13(a), and as anticipated from the results observed in Figure 6(a), increasing the oscillation frequency from 1 to 2 Hz results in shorter fouling induction times. This is also the case for all studied combinations of temperature and supersaturation studied for L-glutamic acid (i.e. [20°C, S=6], [20°C, S=4] and [30°C, S=4.2]). Higher frequencies increase fluid shear and encourage nucleation on the glass surface at a greater rate [56, 57, 58, 59, 60]. In addition, the results obtained for glycine reveal that increasing the amplitude of the flow oscillation also decreases fouling induction times. The effect is similar to the one observed when the oscillation frequency is raised since increasing the amplitude of the oscillation promotes fluid shear in the system that enhances crystal nucleation. As expected, the combination of increasing the two variables simultaneously has the largest effect on the early appearance of fouling.

For L-glutamic acid, increasing the supersaturation of the solution in the cold straight from S=4 to S=6, decreases the fouling induction time by almost one order of magnitude, independently of the oscillation frequency. As expected, nucleation is faster and therefore shorter fouling induction times are observed at higher supersaturation at a given temperature. The opposite effect is observed when the temperature in the crystallisation straight is increased from 20°C to 30°C at a given solution concentration (i.e. 42.4 g/L). The temperature increase translates into a supersaturation drop from S=6 to S=4.2 that reduces the driving force for crystallisation and hence leads to slower nucleation rates and longer fouling induction times.

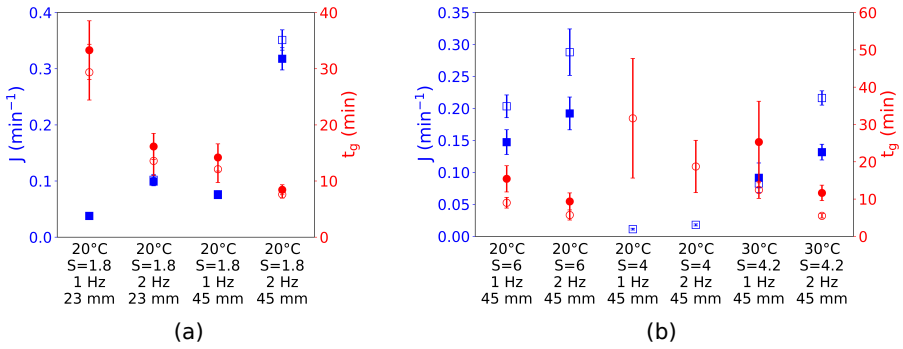

Figure 7: Fouling nucleation rates (blue squares) and growth times (red circles) for (a) glycine and (b) L-glutamic acid aqueous solutions at different levels of supersaturation and oscillatory flow conditions. Closed symbols correspond to results obtained with the automated image processing method while open symbols represent results obtained through visual inspection. The nucleation kinetics parameters for L-glutamic acid at 20°C and S=4 are not displayed for the automated image processing method due to limited number of samples to achieve a representative fit of the Poisson distribution model.

3.3. Nucleation rates and growth times

The Poisson distribution model [55] (Equations 2 and 3) provides a framework to further extract fouling nucleation kinetics from the distribution of fouling induction times. The fits of this model to the cumulative probability distribution of induction times for every experimental condition are shown in Figure C.14 in the Appendix. The estimated values of the nucleation rates J and the growth times t_g are displayed in Figure 7, and summarised in Table C.3 and Table C.4 in the Appendix. It can be noted that changing the frequency by 1 Hz has approximately the same effect on J and t_g as changing the amplitude by 22 mm, as shown in Figure 7(a). This indicates that amplitude and frequency have a synergistic effect in affecting fouling nucleation kinetics. In the case of L-glutamic acid, a similar trend is observed on the effect of frequency on fouling nucleation kinetics, as shown in Figure 7(b).

The combined effect of frequency f and amplitude x_0 of the oscillatory flow on nucleation kinetics can be characterised in terms of the oscillatory Reynolds

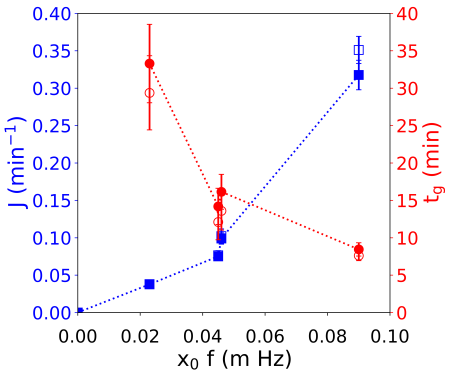

Figure 8: Fouling nucleation rates (blue squares) and growth times (red circles) for glycine aqueous solutions at different oscillatory flow conditions. Closed symbols correspond to results obtained with the automated image processing method while open symbols represent results obtained through visual inspection. For nucleation rates, some of the results obtained with these two methods overlap and some error bars are smaller than the symbol size. Dashed lines are a guide to the eye.

number Re_o [1, 45, 61, 62], given by:

$$Re_o = \frac{2\pi f x_0 \rho d_e}{\mu}, \tag{4}$$

where ρ and μ are the fluid density and dynamic viscosity, respectively, and d_e is the effective tube diameter. For systems at constant temperature and pressure studied within fixed equipment (i.e. constant d_e), the oscillatory Reynolds number is proportional to the product of amplitude and frequency of the oscillatory flow (i.e. $x_0 f$).

Figure 8 shows the effect of $x_0 f$ on fouling nucleation rate and growth time for the glycine system. Good agreement is achieved between visual inspection and automated image processing, with all the results falling within the error bars of the two methods (corresponding to one standard deviation). The fouling nucleation rate and the fouling growth time have a strong but inverse dependence on the product $x_0 f$, and therefore on the oscillatory Reynolds number Re_o. These observations suggest that the oscillatory Reynolds number is a good indicator of the effect of fluid flow on nucleation kinetics in oscillatory

flow crystallisers.

The results of this study are consistent with previous investigations on the effect of fluid shear on crystal nucleation. Yang et al. observed that induction times in the bulk fluid of butyl paraben-ethanol solutions decreased with increasing amplitude and frequency of the oscillatory flow in COBC and MFOBC setups [48]. Forsyth et al. also showed that increasing the shear rate leads to larger nucleation rates and shorter growth times for glycine aqueous solutions in Couette and capillary flow setups [59]. Furthermore, using Couette cells, primary nucleation kinetics were shown to increase with larger glass-liquid interfacial areas [60], indicating that heterogeneous nucleation on glass surfaces would be the predominant mechanism for primary nucleation. Since the oscillatory Reynolds number is proportional to the peak shear rate, a similar scenario is expected in COBC and MFOBC setups. The highest primary nucleation rates occur where shear rates are the highest, leading to onset of fouling on the walls of the crystalliser and inducing subsequent secondary nucleation in the bulk liquid. While previous work hypothesised this scenario based on indirect observations [48, 60], here we validate this insight through direct measurements of heterogeneous nucleation on the wall of the crystalliser.

4. Conclusions

The influence of oscillatory flow conditions on the occurrence of fouling is studied here for the first time in oscillatory baffled crystallisers. The fouling phenomena expected in the COBC are reproduced in the compact MFOBC, reducing the consumption of materials and energy during the experiments. A non-invasive and automated imaging method based on commodity web cameras is used to capture fouling events and determine fouling induction times in glycine and L-glutamic acid aqueous solutions. The results are validated through visual inspection and the imaging technique is shown to be sensitive enough to provide timely early warnings of fouling in the system.

This paper shows that higher frequencies and larger amplitudes of the flow

oscillation result in increased fluid shear that promotes heterogeneous nucleation on the crystalliser walls, leading to fouling. A Poisson distribution model is used to determine fouling nucleation kinetics from the distribution of induction times. The analysis reveals that increasing the oscillatory Reynolds number leads to increased fouling nucleation rates and shorter growth times, in agreement with previous work investigating effects of fluid shear on primary nucleation.

The results obtained in this work provide further insight to enable better understanding and control of crystal nucleation on the crystalliser walls as a key to ensuring a stable operation in continuous crystallisation processes.

Acknowledgements

This work was performed within the UK EPSRC funded project 'Intelligent Decision Support and Control Technologies for Continuous Manufacturing and Crystallisation of Pharmaceuticals and Fine Chemicals (ICT-CMAC)' (EP/K014250/1) and the EPSRC Centre for Innovative Manufacturing in Continuous Manufacturing and Crystallisation (EP/I033459/1). The authors would like to thank the EPSRC, AstraZeneca and GSK for the financial support and Dr Jerzy Dziewierz for developing the image processing code for visual inspection of fouling events.

References

[1] T. McGlone, N. E. B. Briggs, C. A. Clark, C. J. Brown, J. Sefcik, A. J. Florence, Oscillatory flow reactors (OFRs) for continuous manufacturing and crystallization, Org. Process Res. Dev. 19 (2015) 1186–1202. doi:10.1021/acs.oprd.5b00225.
URL https://doi.org/10.1021/acs.oprd.5b00225

[2] M. Hewgill, M. Mackley, A. Pandit, S. Pannu, Enhancement of gas-liquid mass transfer using oscillatory flow in a baffled tube, Chem. Eng. Sci. 48 (1993) 799–809. doi:10.1016/0009-2509(93)80145-G.

URL http://www.sciencedirect.com/science/article/pii/0009250993801456

[3] X. Ni, S. Gao, R. Cumming, D. Pritchard, A comparative study of mass transfer in yeast for a batch pulsed baffled bioreactor and a stirred tank fermenter, Chem. Eng. Sci. 50 (1995) 2127–2136. doi:10.1016/0009-2509(95)00050-F.
URL https://doi.org/10.1016/0009-2509(95)00050-F

[4] M. Mackley, G. Tweddle, I. Wyatt, Experimental heat transfer measurements for pulsatile flow in baffled tubes, Chem. Eng. Sci. 45 (1990) 1237–1242. doi:10.1016/0009-2509(90)87116-A.
URL https://doi.org/10.1016/0009-2509(90)87116-A

[5] M. Mackley, P. Stonestreet, Heat transfer and associated energy dissipation for oscillatory flow in baffled tubes, Chem. Eng. Sci. 50 (1995) 2211–2224. doi:10.1016/0009-2509(95)00088-M.
URL http://www.sciencedirect.com/science/article/pii/000925099500088M

[6] S. Lawton, G. Steele, P. Shering, L. Zhao, I. Laird, X. W. Ni, Continuous crystallization of pharmaceutical using a continuous oscillatory baffled crystalliser, Org. Process Res. Dev. 13 (2009) 1357–1363. doi:10.1021/op900237x.
URL https://doi.org/10.1021/op900237x

[7] L. Zhao, V. Raval, N. E. B. Briggs, R. M. Bhardwaj, T. McGlone, I. D. H. Oswald, A. J. Florence, From discovery to scale-up: α-lipoic acid:nicotinamide co-crystals in a continuous oscillatory baffled crystalliser, Cryst. Eng. Comm. 16 (2014) 5769–5780. doi:10.1039/C4CE00154K.
URL http://dx.doi.org/10.1039/C4CE00154K

[8] C. J. Brown, J. A. Adelakun, X. Ni, Characterization and modelling of antisolvent crystallization of salicylic acid in a continuous oscillatory

baffled crystallizer, Chem. Eng. Process.: Process Intensification 97 (2015) 180–186. doi:https://doi.org/10.1016/j.cep.2015.04.012.
URL http://www.sciencedirect.com/science/article/pii/S025527011530012X

[9] P. Stonestreet, A. Harvey, A mixing-based design methodology for continuous oscillatory flow reactors, Chem. Eng. Res. Des. 80 (2002) 31–44. doi:10.1205/026387602753393204.
URL https://doi.org/10.1205/026387602753393204

[10] M. S. Abbott, A. P. Harvey, G. V. Perez, M. K. Theodorou, Biological processing in oscillatory baffled reactors: operation, advantages and potential, Interface Focus 3 (2013) 20120036. doi:10.1098/rsfs.2012.0036.
URL https://doi.org/10.1098/rsfs.2012.0036

[11] N. E. B. Briggs, J. McGinty, C. McCabe, V. Raval, J. Sefcik, A. J. Florence, Heat transfer and residence time distribution in plug flow continuous oscillatory baffled crystallizers, ACS Omega 6 (28) (2021) 18352–18363. doi:10.1021/acsomega.1c02215.
URL https://doi.org/10.1021/acsomega.1c02215

[12] J. W. Mullin, Crystallization, 4th Edition, Butterworth-Heinemann, 2001.
URL https://www.elsevier.com/books/crystallization/mullin/978-0-7506-4833-2

[13] L. L. Simon, E. Simone, K. A. Oucherif, Crystallization process monitoring and control using process analytical technology, in: R. Singh, Z. Yuan (Eds.), Process Systems Engineering for Pharmaceutical Manufacturing, Vol. 41 of Computer Aided Chemical Engineering, Elsevier, 2018, Ch. 9, pp. 215–242. doi:10.1016/B978-0-444-63963-9.00009-9.
URL https://doi.org/10.1016/B978-0-444-63963-9.00009-9

[14] S. Prakash, N. Datta, H. C. Deeth, Methods of detecting fouling caused by heating of milk, Food Rev. Int. 21 (2005) 267–293. doi:10.1080/

FRI-200061609.
URL https://doi.org/10.1080/FRI-200061609

[15] E. Wallhäußer, M. Hussein, T. Becker, Detection methods of fouling in heat exchangers in the food industry, Food Control 27 (2012) 1–10. doi:10.1016/j.foodcont.2012.02.033.
URL https://doi.org/10.1016/j.foodcont.2012.02.033

[16] L. D. Tijing, Y. C. Woo, J.-S. Choi, S. Lee, S.-H. Kim, H. K. Shon, Fouling and its control in membrane distillation — a review, J. Membrane Sci. 475 (2018) 215–244. doi:10.1016/j.memsci.2014.09.042.
URL https://doi.org/10.1016/j.memsci.2014.09.042

[17] A. O. Olufade, C. J. Simonson, Characterization of the evolution of crystallization fouling in membranes, ACS Omega 3 (2018) 17188–17198. doi:10.1021/acsomega.8b01058.
URL https://doi.org/10.1021/acsomega.8b01058

[18] S. Suwal, A. Doyen, L. Bazinet, Characterization of protein, peptide and amino acid fouling on ion-exchange and filtration membranes: Review of current and recently developed methods, J. Membrane Sci. 496 (2015) 267–283. doi:10.1016/j.memsci.2015.08.056.
URL https://doi.org/10.1016/j.memsci.2015.08.056

[19] M. Britten, M. L. Green, M. Boulet, P. Paquin, Deposit formation on heated surfaces: Effect of interface energetics, J. Dairy Res. 55 (1988) 551–562. doi:10.1017/S0022029900033331.
URL https://doi.org/10.1017/S0022029900033331

[20] J. P. Tissier, M. Lalande, Experimental device and methods for studying milk deposit formation on heat exchange surfaces, Biotechnol. Progr. 2 (1986) 218–229. doi:10.1002/btpr.5420020410.
URL https://doi.org/10.1002/btpr.5420020410

[21] M. Mayer, J. Bucko, W. Benzinger, R. Dittmeyer, W. Augustin, S. Scholl, The impact of crystallization fouling on a microscale heat exchanger, Exp. Therm. Fluid Sci. 40 (2012) 126–131. doi:10.1016/j.expthermflusci.2012.02.007.
URL https://doi.org/10.1016/j.expthermflusci.2012.02.007

[22] C. Riverol, V. Napolitano, Estimation of fouling in a plate heat exchanger through the application of neural networks, J. Chem Technol. Biot. 80 (2005) 594–600. doi:10.1002/jctb.1198.
URL https://doi.org/10.1002/jctb.1198

[23] M. G. Mwaba, M. R. Golriz, J. Gu, A semi-empirical correlation for crystallization fouling on heat exchange surfaces, Appl. Therm. Eng. 26 (2006) 440–447. doi:10.1016/j.applthermaleng.2005.05.021.
URL https://doi.org/10.1016/j.applthermaleng.2005.05.021

[24] T. M. Pääkkönen, M. Riihimäki, C. J. Simonson, E. Muurinen, R. L. Keiski, Crystallization fouling of $CaCO_3$ – Analysis of experimental thermal resistance and its uncertainty, Int. J. Heat Mass Tran. 55 (2012) 6927–6937. doi:10.1016/j.ijheatmasstransfer.2012.07.006.
URL https://doi.org/10.1016/j.ijheatmasstransfer.2012.07.006

[25] J.-S. Park, J.-H. Choi, K.-H. Yeon, S.-H. Moon, An approach to fouling characterization of an ion-exchange membrane using current-voltage relation and electrical impedance spectroscopy, J. Colloid Interf. Sci. 294 (2006) 129–138. doi:10.1016/j.jcis.2005.07.016.
URL https://doi.org/10.1016/j.jcis.2005.07.016

[26] X. D. Chen, D. X. Y. Li, S. X. Q. Lin, N. Özkan, On-line fouling/cleaning detection by measuring electric resistance – equipment development and application to milk fouling detection and chemical cleaning monitoring, J. Food Eng. 61 (2004) 181–189. doi:10.1016/S0260-8774(03)00085-2.
URL https://doi.org/10.1016/S0260-8774(03)00085-2

[27] P. M. Withers, Ultrasonic, acoustic and optical techniques for the non-invasive detection of fouling in food processing equipment, Trends Food Sci. Tech. 7 (1996) 293–298. doi:10.1016/0924-2244(96)10031-5.
URL https://doi.org/10.1016/0924-2244(96)10031-5

[28] E. Wallhäußer, W. B. Hussein, M. A. Hussein, J. Hinrichs, T. M. Becker, On the usage of acoustic properties combined with an artificial neural network – a new approach of determining presence of dairy fouling, J. Food Eng. 103 (2011) 449–456. doi:10.1016/j.jfoodeng.2010.11.015.
URL https://doi.org/10.1016/j.jfoodeng.2010.11.015

[29] A. O. Olufade, C. J. Simonson, Application of indirect non-invasive methods to detect the onset of crystallization fouling in a liquid-to-air membrane energy exchanger, Int. J. Heat Mass Tran. 127 (2018) 663–673. doi:10.1016/j.ijheatmasstransfer.2018.06.032.
URL https://doi.org/10.1016/j.ijheatmasstransfer.2018.06.032

[30] Z. K. Nagy, G. Fevotte, H. Kramer, L. L. Simon, Recent advances in the monitoring, modelling and control of crystallization systems, Chem. Eng. Res. Des. 91 (2013) 1903–1922. doi:10.1016/j.cherd.2013.07.018.
URL https://doi.org/10.1016/j.cherd.2013.07.018

[31] J. Cardona, C. Ferreira, J. McGinty, A. Hamilton, O. S. Agimelen, A. Cleary, R. Atkinson, C. Michie, S. Marshall, Y.-C. Chen, J. Sefcik, I. Andonovic, C. Tachtatzis, Image analysis framework with focus evaluation for in situ characterisation of particle size and shape attributes, Chem. Eng. Sci. 191 (2018) 208–231. doi:10.1016/j.ces.2018.06.067.
URL https://doi.org/10.1016/j.ces.2018.06.067

[32] A. Borsos, B. Szilágy, P. Ş. Agachi, Z. K. Nagy, Real-time image processing based online feedback control system for cooling batch crystallization, Org. Process Res. Dev. 21 (2017) 511–519. doi:10.1021/acs.oprd.6b00242.
URL https://doi.org/10.1021/acs.oprd.6b00242

[33] H. Qu, M. Louhi-Kultanen, J. Kallas, In-line image analysis on the effects of additives in batch cooling crystallization, Cryst. Growth Des. 289 (2006) 286–294. doi:10.1016/j.jcrysgro.2005.11.108.
URL https://doi.org/10.1016/j.jcrysgro.2005.11.108

[34] L. L. Simon, K. Z. Nagy, K. Hungerbuhler, Endoscopy-based in situ bulk video imaging of batch crystallization processes, Org. Process Res. Dev. 13 (2009) 1254–1261. doi:10.1021/op900019b.
URL https://doi.org/10.1021/op900019b

[35] Y. Zhou, R. Srinivasan, S. Lakshminarayanan, Critical evaluation of image processing approaches for real-time crystal size measurements, Comput. Chem. Eng. 33 (2009) 1022–1035. doi:10.1016/j.compchemeng.2008.10.021.
URL https://doi.org/10.1016/j.compchemeng.2008.10.021

[36] M. Jiang, R. D. Braatz, Low-cost noninvasive real-time imaging for tubular continuous-flow crystallization, Chem. Eng. Technol. 41 (2018) 143–148. doi:10.1002/ceat.201600276.
URL https://doi.org/10.1002/ceat.201600276

[37] P. Neugebauer, J. Cardona, M. O. Besenhard, A. Peter, H. Gruber-Woelfler, C. Tachtatzis, A. Cleary, I. Andonovic, J. Sefcik, J. G. Khinast, Crystal shape modification via cycles of growth and dissolution in a tubular crystallizer, Cryst. Growth Des. 18 (2018) 4403–4415. doi:10.1021/acs.cgd.8b00371.
URL https://doi.org/10.1021/acs.cgd.8b00371

[38] L. L. Simon, Z. K. Nagy, K. Hungerbuhler, Comparison of external bulk video imaging with focused beam reflectance measurement and ultra-violet visible spectroscopy for metastable zone identification in food and pharmaceutical crystallization processes, Chem. Eng. Sci. 64 (2009) 3344–3351. doi:10.1016/j.ces.2009.04.016.
URL https://doi.org/10.1016/j.ces.2009.04.016

[39] X. Z. Wang, K. J. Roberts, C. Ma, Crystal growth measurement using 2D and 3D imaging and the perspectives for shape control, Chem. Eng. Sci. 63 (2008) 1173–1184. doi:10.1016/j.ces.2007.07.018.
URL https://doi.org/10.1016/j.ces.2007.07.018

[40] M. Kempkes, T. Vetter, M. Mazzotti, Measurement of 3D particle size distributions by stereoscopic imaging, Chem. Eng. Sci. 65 (2010) 1362–1373. doi:10.1016/j.ces.2009.10.008.
URL https://doi.org/10.1016/j.ces.2009.10.008

[41] S. Schorsch, T. Vetter, M. Mazzotti, Measuring multidimensional particle size distributions during crystallization, Chem. Eng. Sci. 77 (2012) 130–142. doi:10.1016/j.ces.2011.11.029.
URL https://doi.org/10.1016/j.ces.2011.11.029

[42] S. Schorsch, D. R. Ochsenbein, T. Vetter, M. Morari, M. Mazzotti, High accuracy online measurement of multidimensional particle size distributions during crystallization, Chem. Eng. Sci. 105 (2014) 155–168. doi:10.1016/j.ces.2013.11.003.
URL https://doi.org/10.1016/j.ces.2013.11.003

[43] R. Zhang, C. Y. Ma, J. J. Liu, X. Z. Wang, On-line measurement of the real size and shape of crystals in stirred tank crystalliser using non-invasive stereo vision imaging, Chem. Eng. Sci. 137 (2015) 9–21. doi:10.1016/j.ces.2015.05.053.
URL https://doi.org/10.1016/j.ces.2015.05.053

[44] A. K. Rajagopalan, J. Schneeberger, F. Salvatori, S. Bötschi, D. R. Ochsenbein, M. R. Oswald, M. Pollefeys, M. Mazzotti, A comprehensive shape analysis pipeline for stereoscopic measurements of particulate populations in suspension, Powder Technol. 321 (2017) 479–493. doi:10.1016/j.powtec.2017.08.044.
URL https://doi.org/10.1016/j.powtec.2017.08.044

[45] L. N. Ejim, S. Yerdelen, T. McGlone, I. Onyemelukwe, B. Johnston, A. J. Florence, N. M. Reis, A factorial approach to understanding the effect of inner geometry of baffled meso-scale tubes on solids suspension and axial dispersion in continuous, oscillatory liquid–solid plug flows, Chem. Eng. J. 308 (2017) 669–682. doi:10.1016/j.cej.2016.09.013.
URL https://doi.org/10.1016/j.cej.2016.09.013

[46] C. J. Brown, X. Ni, Online evaluation of paracetamol antisolvent crystallization growth rate with video imaging in an oscillatory baffled crystallizer, Cryst. Growth Des. 11 (2011) 719–725. doi:10.1021/cg1011988.
URL https://doi.org/10.1021/cg1011988

[47] C. J. Brown, X. Ni, Evaluation of growth kinetics of antisolvent crystallization of paracetamol in an oscillatory baffled crystallizer utilizing video imaging, Cryst. Growth Des. (2011) 3994–4000doi:10.1021/cg200560b.
URL https://doi.org/10.1021/cg200560b

[48] H. Yang, X. Yu, V. Raval, Y. Makkawi, A. Florence, Effect of oscillatory flow on nucleation kinetics of butyl paraben, Cryst. Growth Des. 16 (2016) 875–886. doi:10.1021/acs.cgd.5b01437.
URL https://doi.org/10.1021/acs.cgd.5b01437

[49] C. Tachtatzis, R. Sheridan, C. Michie, R. C. Atkinson, A. Cleary, J. Dziewierz, I. Andonovic, N. Briggs, A. J. Florence, J. Sefcik, Image-based monitoring for early detection of fouling in crystallisation processes, Chem. Eng. Sci. 133 (2015) 82–90. doi:10.1016/j.ces.2015.01.038.
URL https://doi.org/10.1016/j.ces.2015.01.038

[50] N. Briggs, Polymorph control of pharmaceuticals within a continuous oscillatory baffled crystalliser, Phd thesis (2015).
URL http://oleg.lib.strath.ac.uk/R/?func=dbin-jump-full&object_id=26054

[51] M. Jelinska-Kazimierczuk, J. Szydlowski, Isotope effect on the solubility of amino acids in water, J. Solution Chem. 25 (1996) 1175–1184. doi:

10.1007/BF00972645.
URL https://doi.org/10.1007/BF00972645

[52] H. D. Belitz, W. Grosch, P. Schieberle, Food Chemistry, 4th Edition, Springer-Verlag Berlin Heidelberg, 2009. doi:10.1007/978-3-540-69934-7.
URL https://www.springer.com/gp/book/9783540699330

[53] E. Manzurola, A. Apelblat, Solubilities of L-glutamic acid, 3-nitrobenzoic acid, p-toluic acid, calcium-L-lactate, calcium gluconate, magnesium-DL-asparate, and magnesium-L-lactate in water, J. Chem. Thermodyn. 34 (2002) 1127–1136. doi:10.1006/jcht.2002.0975.
URL https://doi.org/10.1006/jcht.2002.0975

[54] M. Lundvall, Yawcam, yet another webcam software (2013).
URL https://www.yawcam.com/

[55] S. Jiang, J. H. ter Horst, Crystal nucleation rates from probability distributions of induction times, Cryst. Growth Des. 11 (2011) 256–261. doi:10.1021/cg101213q.
URL https://doi.org/10.1021/cg101213q

[56] G. Kumaraswamy, A. M. Issaian, J. A. Kornfield, Shear-enhanced crystallization in isotactic polypropylene. 1. correspondence between in situ rheo-optics and ex situ structure determination, Macromolecules 32 (1999) 7537–7547. doi:10.1021/ma990772j.
URL https://doi.org/10.1021/ma990772j

[57] E. Koscher, R. Fulchiron, Influence of shear on polypropylene crystallization: morphology development and kinetics, Polymer 43 (2002) 6931–6942. doi:10.1016/S0032-3861(02)00628-6.
URL https://doi.org/10.1016/S0032-3861(02)00628-6

[58] A. Jawor-Baczynska, B. D. Moore, J. Sefcik, Effect of mixing, concentration and temperature on the formation of mesostructured solutions and their

role in the nucleation of DL-valine crystals, Faraday Discuss. 179 (2015) 141–154. doi:10.1039/C4FD00262H.
URL http://dx.doi.org/10.1039/C4FD00262H

[59] C. Forsyth, P. A. Mulheran, C. Forsyth, M. D. Haw, I. S. Burns, J. Sefcik, Influence of controlled fluid shear on nucleation rates in glycine aqueous solutions, Cryst. Growth Des. 15 (2015) 94–102. doi:10.1021/cg5008878.
URL https://doi.org/10.1021/cg5008878

[60] C. Forsyth, I. S. Burns, P. A. Mulheran, J. Sefcik, Scaling of glycine nucleation kinetics with shear rate and glass-liquid interfacial area, Cryst. Growth Des. 16 (2016) 136–144. doi:10.1021/acs.cgd.5b01042.
URL https://doi.org/10.1021/acs.cgd.5b01042

[61] X. Ni, P. Gough, On the discussion of the dimensionless groups governing oscillatory flow in a baffled tube, Chem. Eng. Sci. 52 (1997) 3209–3212. doi:10.1016/S0009-2509(97)00104-8.
URL https://doi.org/10.1016/S0009-2509(97)00104-8

[62] N. E. B. Briggs, U. Schacht, V. Raval, T. McGlone, J. Sefcik, A. J. Florence, Seeded crystallization of β-L-glutamic acid in a continuous oscillatory baffled crystallizer, Org. Process Res. Dev. 19 (2015) 1903–1911. doi:10.1021/acs.oprd.5b00206.
URL https://doi.org/10.1021/acs.oprd.5b00206

Appendix A. Temperature profiles

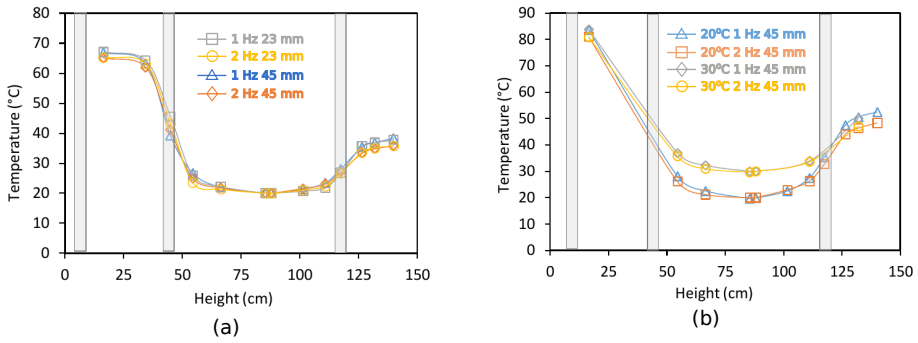

Figure A.9: Temperature profiles in the MFOBC for: (a) glycine aqueous solutions at 385 g/L and a crystallisation temperature of 20 °C and (b) L-glutamic acid aqueous solutions at 42.4 g/L. The vertical bars represent the position of the PTFE collars in the MFOBC.

Appendix B. Determination of fouling induction times

Figure B.10: Example of 5 consecutive frames from a glycine experiment at 20°C and 385 g/L (S=1.8) with an oscillation frequency of 1 Hz and amplitude of 23 mm. The outlier observed in the central frame was detected and discarded by the image analysis algorithm due to lack of persistence of the bright signal.

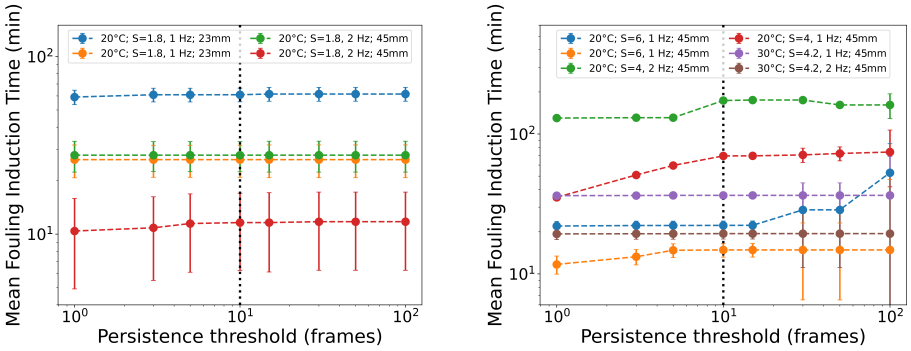

(a) Glycine (b) L-glutamic acid

Figure B.11: Effect of persistence threshold on mean fouling induction times obtained with the automated image processing method for (a) glycine and (b) L-glutamic acid aqueous solutions. The dotted black line indicates the selected persistence threshold (i.e. the pixel intensity remains above the fouling detection threshold for longer than 10 consecutive frames). Dashed lines are a guide to the eye.

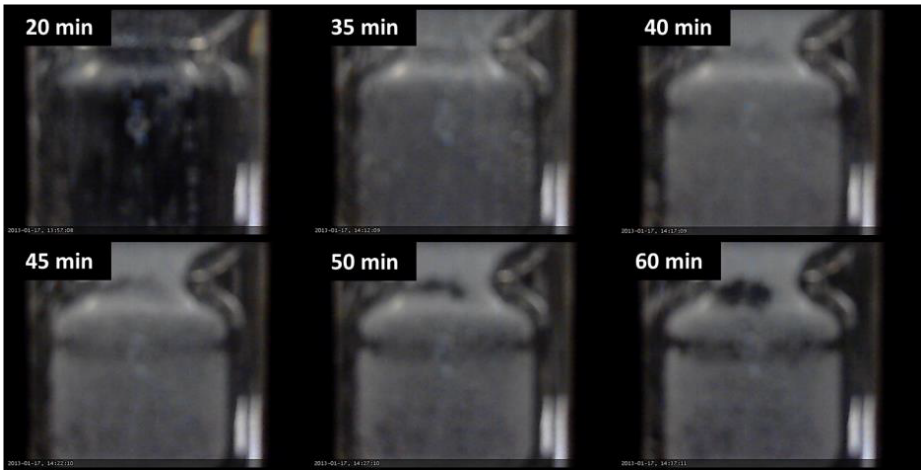

Figure B.12: Example of an event of encrustation detachment over time after extensive fouling has occurred during an L-glutamic acid experiment.

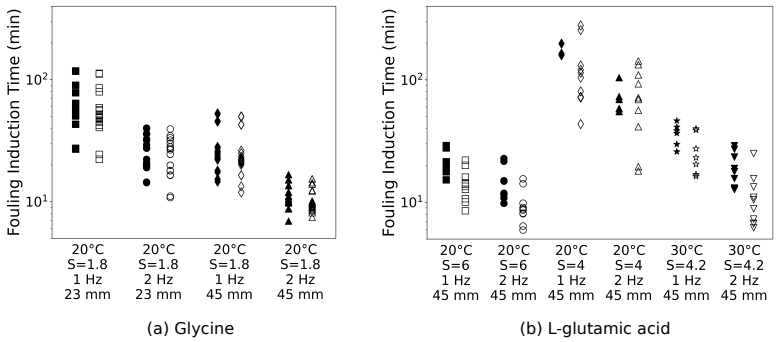

Figure B.13: Effect of oscillation conditions, temperature and concentration on fouling induction times of (a) glycine and (b) L-glutamic acid aqueous solutions. Closed symbols correspond to results obtained with the automated image processing method while open symbols represent results obtained through visual inspection.

Appendix C. Fouling nucleation and growth kinetics

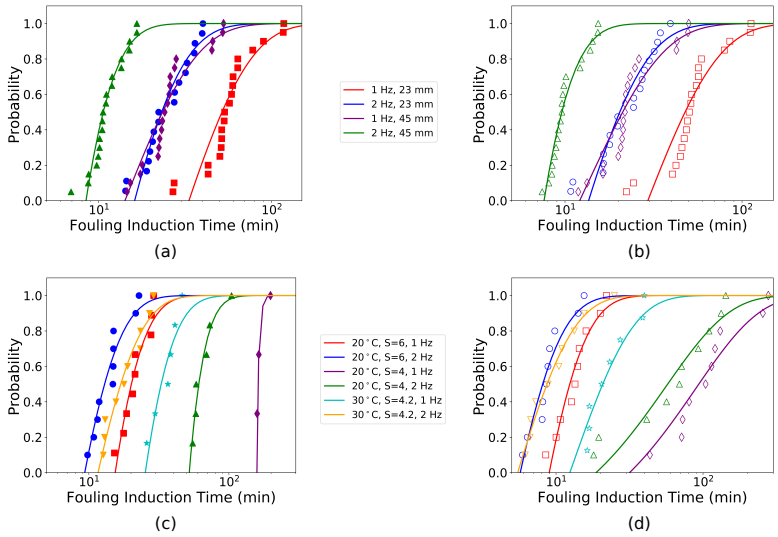

Figure C.14: Cumulative probability distributions of fouling induction times for glycine: (a) automated image processing method and (b) visual inspection method; and L-glutamic acid: (c) automated image processing method and (d) visual inspection method. Symbols represent experimental data while solid lines show the corresponding Poisson distribution fits.

Operating conditions		Nucleation rate J (min^{-1})		Growth time t_g (min)	
f (Hz)	x_0 (mm)	Visual	Automated	Visual	Automated
1	23	0.038 ± 0.003	0.038 ± 0.003	29 ± 5	33 ± 6
2	23	0.102 ± 0.01	0.099 ± 0.007	14 ± 3	16 ± 3
1	45	0.076 ± 0.006	0.075 ± 0.006	12 ± 3	14 ± 3
2	45	0.35 ± 0.02	0.32 ± 0.02	8 ± 1	8 ± 1

Table C.3: Fouling nucleation rates and growth times for for 385 g/L glycine solutions at 20 °C (S=1.8) using both the visual inspection and the automated image processing methods.

Operating conditions			Nucleation rate J (min^{-1})		Growth time t_g (min)	
T (°C)	S	f (Hz)	Visual	Automated	Visual	Automated
20	6	1	0.20 ± 0.02	0.15 ± 0.02	9 ± 2	15 ± 4
20	6	2	0.29 ± 0.04	0.19 ± 0.03	6 ± 2	9 ± 3
20	4	1	0.011 ± 0.001	–	30 ± 20	–
20	4	2	0.018 ± 0.002	–	19 ± 8	–
30	4.2	1	0.083 ± 0.007	0.09 ± 0.03	12 ± 3	30 ± 11
30	4.2	2	0.22 ± 0.02	0.13 ± 0.02	5 ± 1	12 ± 3

Table C.4: Fouling nucleation rates and growth times for L-glutamic acid experiments using both the visual inspection and the automated image processing methods. The nucleation kinetics parameters at 20°C and S=4 are not displayed for the automated image processing method due to limited number of samples to achieve a representative fit of the Poisson distribution model.